A Circuit-Based Approach for Electro-Thermal Modeling of Lithium-Ion Batteries

Maryam Yazdanpour [1], Peyman Taheri [1], Abraham Mansouri [2], Ben Schweitzer [3]

[1] Laboratory for Alternative Energy Conversion (LAEC), School of Mechatronic Systems Engineering, Simon Fraser University, Surrey, BC V3T 0A3, Canada

[2] Department of Mechanical Engineering, American University in Dubai, Dubai, 28282, UAE

[3] AllCell Technologies, Chicago, Illinois 60609, USA

[1]E-mail: myazdanp@sfu.ca

***Abstract*—A two-dimensional electro-thermal model has been developed to provide a tool that can be used to gain a better understanding of dynamic behaviour of lithium-ion (Li-ion) batteries. The model incorporates an equivalent circuit model (ECM) and a coupled electro-thermal model to simulate the non-uniform heat generation rate, the temperature distribution, and the voltage response of the Li-ion cell across variety of operating conditions. The ECM is comprised of two resistance-capacitance (RC) networks, one sires resistor, and one voltage source that are all function of state-of-charge (SOC) and temperature (T). Hybrid pulse power characterization (HPPC) test is applied to extract the ECM parameters at different ambient temperature. The simulations results of the cell model under constant current discharge tests show a good agreement with the experimental data at different environmental temperature. The developed model can be employed for battery thermal management system (BTMS) and battery management system (BMS) design with a light computational demand.**

Battery thermal modelling, Lithium-ion battery, Electro-thermal model, Equivalent-circuit-model

I. Introduction

Li-ion batteries have been identified as a promising solution to meet the increasing demands for alternative energy in electric and hybrid electric vehicles (EVs and HEVs) (1). Among various types of energy storage solutions, Li-ion batteries feature relatively high power and high specific energy, high operating voltage, longevity, and low self-discharge rates (2).

Safety issues and cost (related to cycle and calendar life) are the main obstacles to the development of large fleets of vehicles on public roads equipped with Li-ion batteries. Li-ion batteries can generate a large amount of heat while in use especially at severe discharge rates and high temperature which involve high rate of exothermic electrochemical reactions and Joule heating. Such excessive heat, if not removed appropriately from the battery pack, can cause shortened battery life, thermal runaway, electrolyte fire, and in extreme cases explosions. Moreover,eexposure of Li-ion batteries to sub-freezing environment drastically reduces their energy and power delivery.

Hence, for optimal performance, the battery pack should operate within a controlled temperature range, ideally 20°C - 40°C, and temperature distribution along the cells and across the module should be as uniform as possible. Hence, the development and implementation of Li-ion batteries, particularly in automotive applications, requires a substantial diagnostic and practical modeling efforts to fully understand the thermal characteristics in the batteries across various operating conditions (3; 4; 5). Thermal modeling prompts an

understanding of the battery thermal behaviour beyond what is possible from the experiments and it can provide a basis for exploring thermal management strategies for batteries in hybrid electric vehicles (HEVs) and electric vehicles (EVs) (6).

To accurately predict the thermal response of the Li-ion batteries across variety of operating conditions, it is essential to evaluate the pattern and magnitude of heat generation and heat diffusion inside the cell. This can be done through a physics-based thermo-electrochemical models; nonetheless, such detailed models are mostly recommended for cell design and optimization purposes due to their high fidelity, and they are not practical for real-time applications due to their high order of complexity. Alternatively, when a battery exists and the lab-generated data for the battery is available, empirical-based models which mimic the electrochemical performance of the battery can be developed. The simplicity of robustness of such models enables them to be applied in real-time embedded systems. Equivalent circuit models (ECMs) (7; 8), and fitting function models (9), which is a simplified version of ECMs, are common methodologies in this categories. In our previous works (10; 11; 12) the fitting function approach was applied to develop analytical tools for thermal simulation of Li-ion batteries. This paper that forms a sequel to our previous works, the ECM approach is employed to provide a comprehensive model for simulating the distributed electro-thermal response of the Li-ion batteries across variety of operating conditions.

II. Formulation of the Problem

Figure 1a schematically shows the core of a pouch-type lithium-ion battery that is constructed of several cell assemblies, also known as electrode assemblies. In Fig. 1b, a single cell assembly is depicted. For better illustration, different layers in the cell assembly are shown separated while in the actual battery these layers are compressed; see Fig. 1b. Each cell assembly includes a negative electrode, two layers of separator sheets, and a positive electrode. The electrodes include active materials, required in the battery chemistry, coated on both sides of current collector foils. In most Li-ion batteries, the current collector in positive and negative electrodes are foils of aluminum and copper, respectively. The separator sheet is an electrically inert membrane for transportation of cations (Li^+) between the electrodes. All layers, except current collectors, are porous and are soaked in a concentrated electrolyte liquid. The electrode tabs are the current collector foils extending outside the electrode plates for the purpose of electrical connection, and they are not covered by active materials. Arrows in Fig. 1b present current streamlines during discharge processes. The through-plane straight arrows represent the transport of Li^+ between the electrodes, i.e., transfer current. The in-plane arrows in x-y plane represent the transport of charges (e^-), i.e., the electrical current, on the electrode layers. The direction of transfer and electric currents is reversed for a charging process. As shown in the Fig. 1b, electrical constriction occur at the tabs of positive and negative electrodes. For the sake of convenience, the transfer current on both sides of each electrode can be considered to occur on one side of the electrodes. This approach is common in the literature.

A. Electrical model

A dimensional analysis can be performed to show that owing to the small thickness of layers in the cell assembly, compared to their dimensions in x- and y-directions, the distribution of potential in the electrodes is two-dimensional in x-y plane (13). Accordingly, the governing differential equation for the charge balance in each electrodes reads

$$-\nabla \cdot \mathbf{i}_j + \frac{\mathbf{J} \cdot \mathbf{n}_j}{\delta_{\text{elec},j}} = 0 \quad (j = p, n) \tag{1}$$

where $\mathbf{i}_j = \{i_x, i_y, 0\}_j$ is the in-plane current density vector on each electrode ($\mathrm{A\,m^{-2}}$). The subscript j corresponds to domains of the positive electrode Ω_p and the negative electrode Ω_n. The reaction current density vector on the electrodes is $\mathbf{J} = \{J_x, J_y, J\}$ in ($\mathrm{A\,m^{-2}}$), where J_x and J_y are side reactions and are considered to be negligible. The through-plane component of the reaction current, J, referred to as transfer current, corresponds to the intercalation of lithium

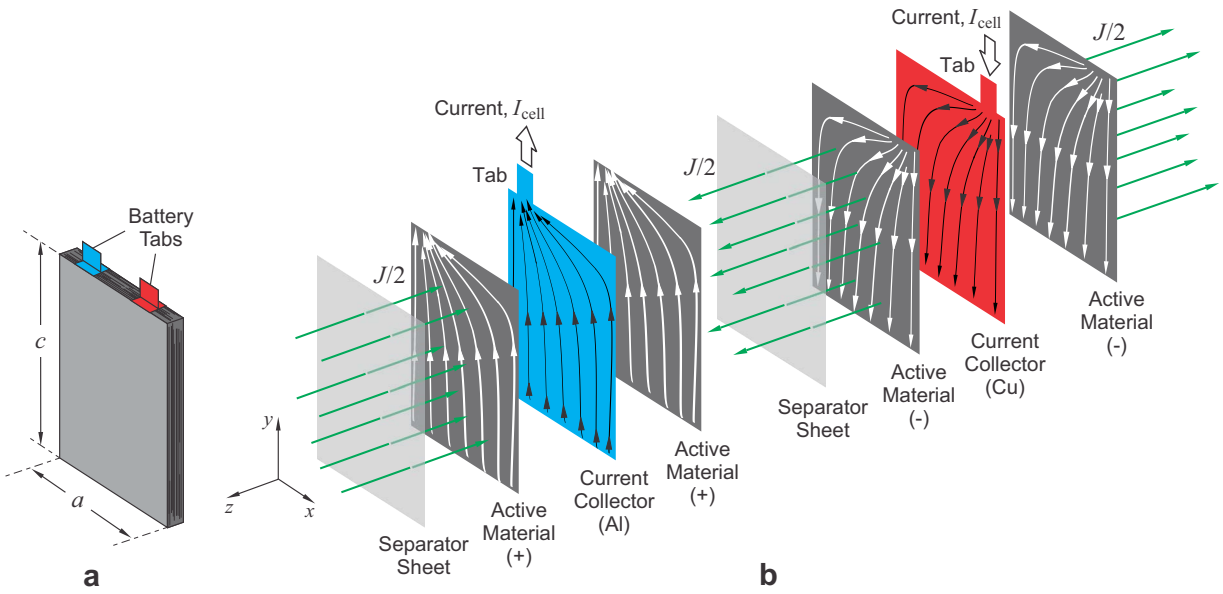

Fig. 1. a) Core (electrode-separator stack) of a pouch-type lithium-ion battery is shown. b) Schematic of a single cell assembly in the battery is shown. The battery core is constructed by repeating the cell assembly. Different layers of the cell are separated for the sake of presentation. The arrows in z-direction correspond to transfer current, the transport of Li^+ from the negative electrode to the positive electrode during a discharge process. The arrows in x-y plane represent current streamlines on electrodes.

ions in active materials on both sides of the electrodes. The electrode thickness in z-direction is $\delta_{\mathrm{elec},j}$ in (m), and $\mathbf{n}_j$ is the unit normal vector on each electrode surface pointing outward; $\mathbf{n}_p = \{0,0,-1\}$ and $\mathbf{n}_n = \{0,0,+1\}$.

According to the Ohm's law, components of $\mathbf{i}_j$ are related to the potential distribution via

$$i_{x,j} = -\sigma_{\mathrm{eff},j}\frac{\partial \Phi_j}{\partial x} \quad \text{and} \quad i_{y,j} = -\sigma_{\mathrm{eff},j}\frac{\partial \Phi_j}{\partial y} \quad (j = p,n) \quad (2)$$

where x and y indicate the spatial position (m), and $\Phi_j = \Phi_j(x,y)$ is the two-dimensional potential distribution in the electrode (V).

The quantity $\sigma_{\mathrm{eff},j}$ is the effective electrical conductivity ($\mathrm{S\,m^{-1}}$), that for each electrode is

$$\sigma_{\mathrm{eff},j} = \frac{1}{\delta_{\mathrm{elec},j}}\left(\delta_{\mathrm{cc},j}\,\sigma_{\mathrm{cc},j} + 2\delta_{\mathrm{am},j}\,\sigma_{\mathrm{am},j}\right) \quad (j = p,n)$$

where

$$\delta_{\mathrm{elec},j} = \delta_{\mathrm{cc},j} + 2\delta_{\mathrm{am},j} \quad (j = p,n)$$

and $\delta_{\mathrm{cc},j}$ and $\delta_{\mathrm{am},j}$ are thicknesses of current collector and active material layers, respectively. Electrical conductivity of the current collector and the active material are denoted by $\sigma_{\mathrm{cc},j}$ and $\sigma_{\mathrm{am},j}$. As depicted in Fig. 2, each electrode

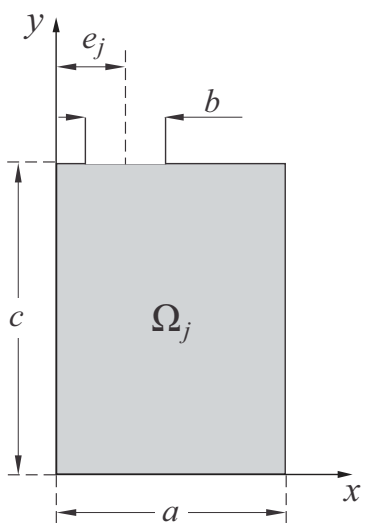

Fig. 2. Two-dimensional schematic of electrodes in x-y plane. Width and height of electrodes and width of the electrode tab are the same for both positive and negative electrodes. The distance of the tab centre from y-axis, denoted by e_j, differs between the electrodes.

can be considered as a rectangular domain in x-y plane of width a and height c. The through-plane current enters (or exits) the domain through its surface in x-y plane, whereas the in-plane current is allowed to exit (or enter) the domain

through the tab constriction of width b on the boundary at $y = c$. The distance between the centre of the tab and y-axis is denoted by e_j.

With reference to Fig. 2, the relevant boundary conditions for Eq. (1) at the positive domain are

$$-\sigma_{\text{eff},p}\frac{\partial \Phi_p}{\partial x} = 0 \quad \text{at} \quad x = 0 \tag{3a}$$

$$-\sigma_{\text{eff},p}\frac{\partial \Phi_p}{\partial x} = 0 \quad \text{at} \quad x = a \tag{3b}$$

$$-\sigma_{\text{eff},p}\frac{\partial \Phi_p}{\partial y} = 0 \quad \text{at} \quad y = 0 \tag{3c}$$

$$-\sigma_{\text{eff},p}\frac{\partial \Phi_p}{\partial y} = i_{\text{tab},p} \quad \text{at} \quad e_p - \frac{b}{2} < x < e_p + \frac{b}{2}, \quad y = c \tag{3d}$$

$$-\sigma_{\text{eff},p}\frac{\partial \Phi_p}{\partial y} = 0 \quad \text{at} \quad e_p + \frac{b}{2} < x < e_p - \frac{b}{2}, \quad y = c \tag{3e}$$

Similarly, for the negative domain

$$-\sigma_{\text{eff},n}\frac{\partial \Phi_n}{\partial x} = 0 \quad \text{at} \quad x = 0 \tag{4a}$$

$$-\sigma_{\text{eff},n}\frac{\partial \Phi_n}{\partial x} = 0 \quad \text{at} \quad x = a \tag{4b}$$

$$-\sigma_{\text{eff},n}\frac{\partial \Phi_n}{\partial y} = 0 \quad \text{at} \quad y = 0 \tag{4c}$$

$$\Phi_n = 0 \quad \text{at} \quad e_n - \frac{b}{2} < x < e_n + \frac{b}{2}, \quad y = c \tag{4d}$$

$$-\sigma_{\text{eff},n}\frac{\partial \Phi_n}{\partial y} = 0 \quad \text{at} \quad e_n + \frac{b}{2} < x < e_n - \frac{b}{2}, \quad y = c \tag{4e}$$

The above boundary conditions imply that no current passes through boundaries of Ω_p and Ω_n except for the tab boundaries. In Eq. (3d), $i_{\text{tab},p}$ is the in-plane current density (A m^{-2}) at the tab of positive electrode

$$i_{\text{tab},p} = \frac{I_{\text{cell}}}{b\,\delta_{\text{elec},p}} \tag{5}$$

where I_{cell} is the applied discharge current (A) for a single cell (electrode) assembly, and $b\,\delta_{\text{elec},p}$ is the cross-sectional area of the positive tab. In Eq. (4d), potential at the tab boundary of the negative electrode is set to zero in order to provide a reference for voltage distribution (14).

B. Equivalent circuit model

Distribution of the transfer current density, J, which appears in the electrical model [cf. Eq. (1)], is dictated by the local rate of electrochemical reactions in electrodes. For an accurate description of J a distributed electrochemical model (6; 13) is preferred. In this study, instead of using an electrochemical model, an equivalent circuit model (15; 16; 17; 18) is employed to predict the time dependent distribution of J in the experimental battery during different operating conditions.

ECMs are the lumped models that utilize the electrical circuit elements to simulate the current-voltage characterizations of the cell with the modest computational effort. A typical circuit is composed of a voltage source representing open-circuit-voltage (OCV), an internal resistance accounting for the ohmic losses, and parallel resistance-capacitor (RC) pairs accounting for activation and concentration polarization of the cell during the operation. The number of RC networks in the equivalent circuit is an important factor that determines the accuracy and complexity of the model. The sufficient number of RC branches in the ECM can be defined from the transient response of the cell voltage during the relaxation phase when the pulse is removed. Normally, the experimental data is fitted to a few equivalent circuits with different number of RC branches and the one that can provide the best match to the experimental data is often selected. The parameters of the ECM are a function of T and SOC of the cell and should be identified from a set of characterization tests conducted at different T and SOC.

Equivalent circuit model development: The cell is characterized by HPPC (19) tests over a range of T and SOCs. In fact the HPPC profile incorporates both charge and discharge pulses to derive the internal resistance and polarization resistances of the cell as a function of SOC with sufficient resolution to reliably establish cell voltage response time constant during discharge, rest, and charge (regen) operating regimes.

The sufficient number of RC-network in the model is determined by fitting the ECM to the transient response of the cell voltage during relaxation phase when the pulse current is halted. The data is separately fitted to three different models: 1) one RC-network pair (first-order ECM), 2) two pairs of RC-network (second-order ECM), and 3) three pairs of RC-network (third-order ECM), the results

are presented in Fig. 3. The R-squared values for fitted model with one, two, and three pairs of RC networks are 0.907, 0.9912, and 0.995, respectively. The results show that one RC-network loop may not produce a satisfactory match to the experimental data. Whereas, the second-order ECM can fit the experimental data with a R-squared value comparable with that of third-order model but with a lower computational cost. Thus, as a compromise between the accuracy and complexity, the model with two pairs of RC-network is selected for this study; the schematic of the considered model is presented in Fig.4.

As shown in Fig. 4, the selected model consists of six components: V_{oc} as cell OCV, an internal resistance, R_0, and two parallel RC-network each consists of one resistance (R_1, R_2) and one capacitor (C_1, C_2), each representing different aspects of the cell. V_{oc} represents the battery open circuit voltage and R_0 is the ohmic or internal resistance of the cell assembly responsible for the immediate voltage drop or rise when the battery is being discharged or charged. Two parallel pairs of RC are responsible for the transient response of the cell. R_1 and C_1 describe the fast dynamics of the cell, depicting the reaction kinetics. R_2 and C_2 represent the slower dynamics of the cell, in the order of hours and are more representative of the diffusion processes in the electrolyte and active material.

The electrical response of the presented circuit can be formulated as:

$$V = V_{\text{OC}} - V_0 - V_1 - V_2 \tag{6}$$

where V_{oc} is a function of SOC that is calculated as;

$$\text{SOC} = \text{SOC}_0 - \frac{1}{\text{cap}_{\text{batt}}} \cdot \int_0^t |I(t)| \cdot dt \tag{7}$$

where Q_{batt} is the nominal capacity of the battery and the constant 3600 has the unit of second/hour. From Kirchhoff's law, three voltage losses terms (V_1, V_2, V_3) can be found as follow:

$$V_0 = I \cdot R_0 \tag{8a}$$

$$\frac{V_1}{R_{\text{eq},1}} + C_{\text{eq},1} \frac{\text{d}V_1}{\text{d}t} = I_{\text{batt}} \tag{8b}$$

$$\frac{V_2}{R_{\text{eq},2}} + C_{\text{eq},2} \frac{\text{d}V_2}{\text{d}t} = I_{\text{batt}} \tag{8c}$$

The parameter estimation consists of two main steps: i) cycling the battery with a standard characterization test, HPPC profile in this study, at different operating temperatures, ii) extracting the parameters from collected experiments. The main goal of the parameter estimation process is to find best possible parameter values to make the model match the experimental data. By iteratively comparing the simulation result against experiment data, the model parameters for the specific operating condition can be found as an optimal fit. The fitting process is performed at each particular SOC and T. Figure. 5 shows a sample of fitting procedure performed at 50% of SOC and 0°C. As reported in Fig. 5, the match between the fitted and measured voltage is excellent with a maximum relative difference (%) between the fitted and measured voltage of 1%.

The results of the parameter estimation are plotted in Fig. 6, which shows the estimated parameters as function of SOC and T. Note that the battery consists of 42 cell assembly units all connected in parallel, while estimated parameters are related to the battery itself, representing the equivalent resistors and capacitors of all 42 units. The resistances and capacitors for each individual cell assembly unit can be calculate based on the equivalent network rule. The equivalent capacitance of the parallel capacitors inside the battery is the sum of the individual capacitance.

$$C_{\text{eq},i} = \sum_{n=1}^{N_{\text{cell}}} C_{n,i} \quad (i = 1,2) \tag{9}$$

The equivalent resistance of resistances connected in parallel is reciprocals of the individual resistances;

$$\frac{1}{R_{\text{eq},i}} = \sum_{n=1}^{N_{\text{cell}}} \frac{1}{R_{n,i}} \qquad (i = 0,1,2) \tag{10}$$

In above equations, it is assumed that the resistance and capacitance of individual cell are identical. By assuming that

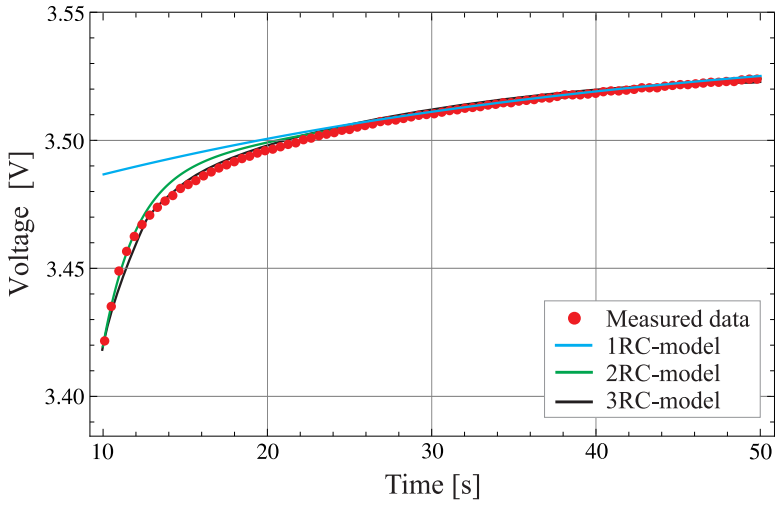

Fig. 3. Fitting the measured voltage (symbols) during relaxation phase (when HPPC pulse is removed) to first-order (blue line), second-order (green line), and third-order (black line) ECM, to determine the optimum number of RC pairs that can accurately describe the voltage behaviour of the experimental battery with the modest computational effort.

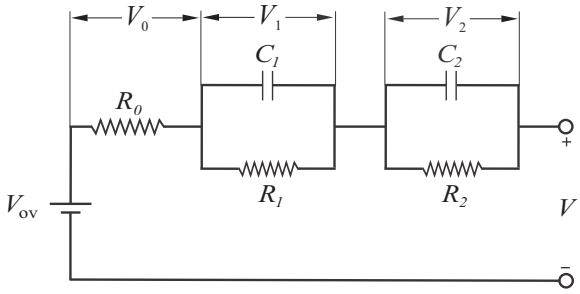

Fig. 4. Schematic of the selected equivalent circuit with two RC-pairs representing a single cell (electrode) assembly.

each cell assembly unit has an identical capacity, the nominal capacity for each unit can be define as;

$$Q_{\text{cell}} = \frac{Q_{\text{batt}}}{N_{\text{cell}}} \tag{11}$$

Similarly, the current passing through each unit cell is;

$$I_{\text{cell}} = \frac{I_{\text{batt}}}{N_{\text{cell}}} \tag{12}$$

In Eqs. (9)-(12), N_{cell} denotes the number of cell assembly units inside the battery.

In the electrode where the electrochemical reaction occurs, local cell voltage from Eq. (6) is the same as the potential difference calculated from the charge balance equations [cf. Eqs. (1) and (2)] (17);

$$V = V_{\text{oc}}(x,y) - V_0(x,y) - V_1(x,y) - V_2(x,y) = \Phi_p(x,y) - \Phi_n(x,y) \tag{13}$$

From Eq. (13), V_0 can be defined as:

$$V_0 = V_{\text{oc}}(x,y) - [\Phi_p(x,y) - \Phi_n(x,y)] - V_1(x,y) - V_2(x,y) \tag{14}$$

from which the reaction current density, J, can be defined as follow;

$$J = \frac{V_0}{R_0\, a\, c} \tag{15}$$

As depicted in Fig. 2, a and b represent the width and the height of the cell, respectively.

C. Thermal model

In the electrical model it was assumed that potential distribution is independent of z-direction. This assumption can be extended to the thermal model as well; since thickness of electrodes in z-direction is very small compared to their dimensions in x- and y-directions, heat will conduct

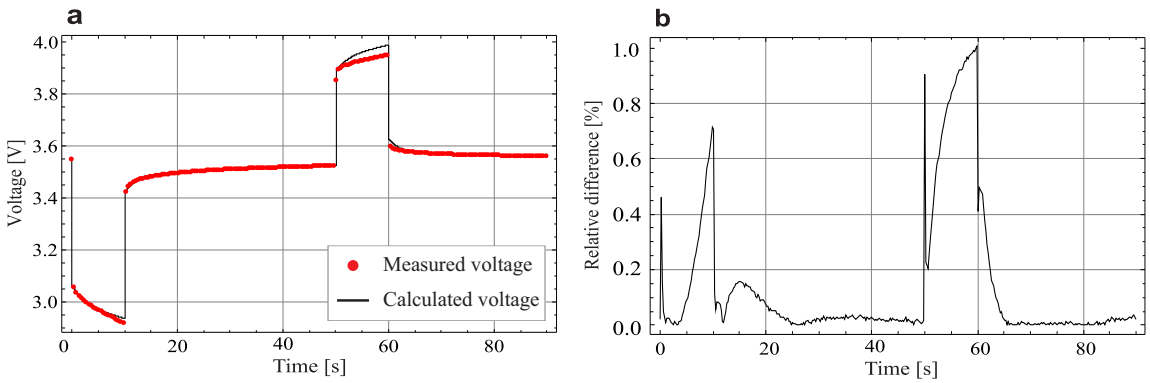

Fig. 5. Results of the parameter estimation process performed at 50% of SOC and 0°C. a) fitted voltage against the measured voltage and b) the relative difference (%) between the measured and fitted data.

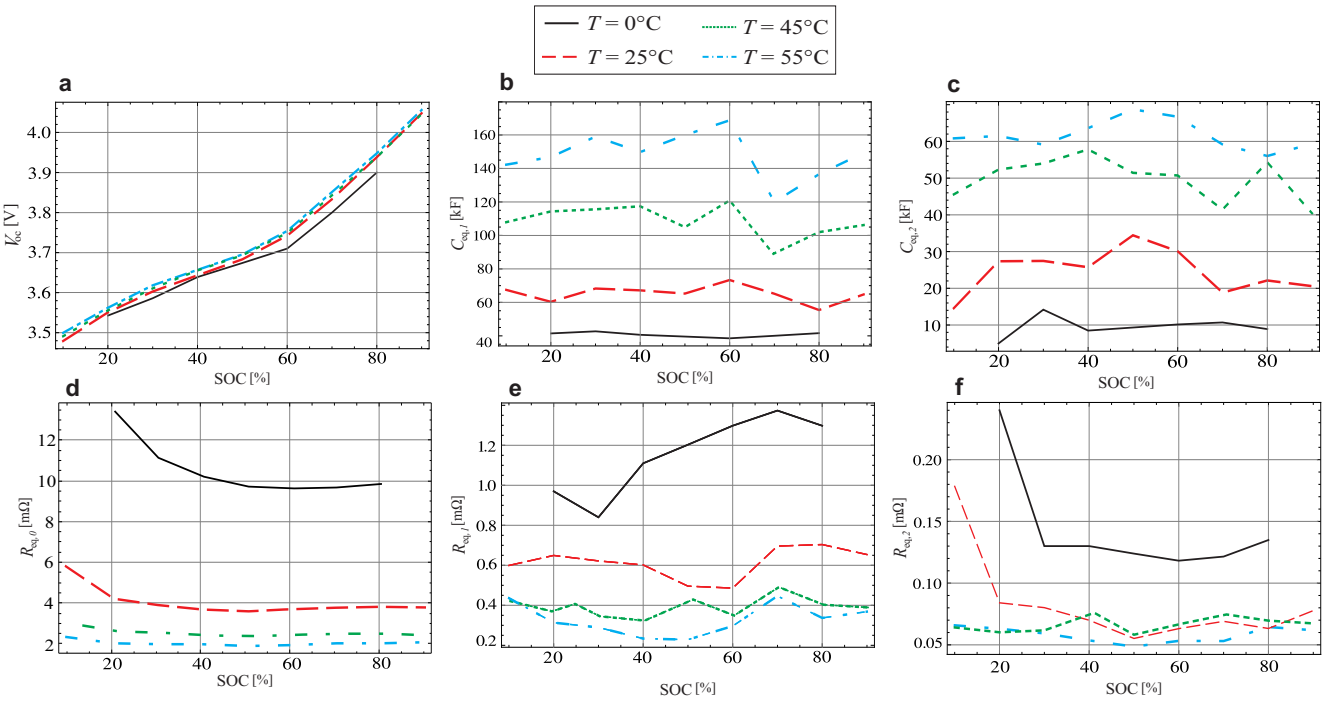

Fig. 6. Results of the parameter estimation process performed at 50% of SOC and 0°C. a) Plotted the fitted voltage against the measured voltage and b) the relative difference (%) between the measured and fitted data.

quickly across the thin direction and the temperature will become, to a good approximation, uniform across z-direction (20; 21). Accordingly, the transient temperature field in the cell assembly is described by a two-dimensional energy equation

$$-\nabla \cdot \mathbf{q} + \dot{g} = \rho c_p \frac{\partial T}{\partial t} \tag{16}$$

where $\mathbf{q} = \{q_x, q_y, 0\}$ is the in-plane heat flux vector on each electrode ($\mathrm{W\,m^{-2}\,K^{-1}}$), $\dot{g}$ is the net rate of volumetric heating inside the battery ($\mathrm{W\,m^{-3}}$), ρ is the density of cell assembly ($\mathrm{kg\,m^{-3}}$), c_p is its specific heat capacity ($\mathrm{J\,kg^{-1}\,K^{-1}}$), t is the time (s), and $T = T(x,y)$ is the two-dimensional temperature distribution in the cell (K).

According to the Fourier's law for heat conduction, components of $\mathbf{q}$ are related to the temperature distribution via

$$q_x = -\kappa_{\mathrm{eff}} \frac{\partial T}{\partial x} \quad \text{and} \quad q_y = -\kappa_{\mathrm{eff}} \frac{\partial T}{\partial y} \tag{17}$$

The quantity κ_{eff} is the effective in-plane thermal conductivity of the cell assembly ($\mathrm{W\,m^{-1}\,K^{-1}}$), calculated from

$$\kappa_{\mathrm{eff}} = \frac{1}{\delta_{\mathrm{cell}}} \left(\delta_{\mathrm{cc},p}\, \kappa_{\mathrm{cc},p} + \delta_{\mathrm{cc},n}\, \kappa_{\mathrm{cc},n} + 2\delta_{\mathrm{am},p}\, \kappa_{\mathrm{am},p} + 2\delta_{\mathrm{am},n}\, \kappa_{\mathrm{am},n} + 2\delta_{\mathrm{ss}}\, \kappa_{\mathrm{ss}} \right)$$

where

$$\delta_{\text{cell}} = \delta_{\text{cc},p} + \delta_{\text{cc},n} + 2\delta_{\text{am},p} + 2\delta_{\text{am},n} + 2\delta_{\text{ss}}$$

with δ_{ss} as the thickness of separator sheet. Thermal conductivities of current collector foils, active materials, and separator sheet are denoted by κ_{cc}, κ_{am}, and κ_{ss}, respectively.

The net rate of volumetric heating inside the battery is the difference between heat generation and heat dissipation rates

$$\dot{g} = \nu_{\text{ec}}\,\dot{g}_{\text{ec}} + \nu_{\text{elec},p}\,\dot{g}_{\text{ohm},p} + \nu_{\text{elec},n}\,\dot{g}_{\text{ohm},n} - \frac{q_{\text{diss}}}{\delta_{\text{cell}}} \qquad (18)$$

where $\dot{g}_{\text{ec}}$ and $\dot{g}_{\text{ohm},j}$ are the electrochemical and ohmic heat generation rates per unit volume. The coefficients ν_{ec} and $\nu_{\text{elec},j}$ are volume ratios for electrochemical and ohmic heat generation rates (22)

$$\nu_{\text{ec}} = \frac{\mathscr{V}_{\text{ec}}}{\mathscr{V}_{\text{cell}}} = \frac{2\delta_{\text{am},p} + 2\delta_{\text{am},n} + 2\delta_{\text{ss}}}{\delta_{\text{cell}}}$$
$$\nu_{\text{elec},j} = \frac{\mathscr{V}_{\text{elec},j}}{\mathscr{V}_{\text{cell}}} = \frac{2\delta_{\text{am},j} + 2\delta_{\text{cc},j}}{\delta_{\text{cell}}} \quad (j = p,n)$$

The quantities $\mathscr{V}_{\text{cell}}$, $\mathscr{V}_{\text{elec},j}$, and $\mathscr{V}_{\text{ec}}$ denote the total volume of the cell assembly, volume of each electrode, and volume of the cell which participates in electrochemical reactions.

The electrochemical heat in each electrode is calculated from (23)

$$\dot{g}_{\text{ec}} = \frac{I_{\text{cell}}}{\mathscr{V}_{\text{cell}}}\left[(V_p - V_n) - V_{\text{oc}} + T\frac{dV_{\text{oc}}}{dT}\right] \qquad (19)$$

where I_{cell} is positive/negative for charge/discharge processes. The last term in Eq. (19) is the reversible heat of electrochemical reactions, while the rest is the irreversible heat due to the cell overpotential. The dependency of the open circuit voltage V_{oc} of the cell on the temperature T at different SOC is demonstrate in Fig. II-C. By assuming a linear dependency between V_{oc} and T, the slope of the V_{oc} curves in Fig. II-C can define the reversible heat coefficient, dV_{oc}/dT. The calculated coefficients vs. SOC are listed in Table. I.

For each electrode, the ohmic (Joulean) heat generation rate reads

$$\dot{g}_{\text{ohm},j} = \frac{1}{\sigma_{\text{eff},j}}(i_{x,j}^2 + i_{y,j}^2) \quad (j = p,n) \qquad (20)$$

TABLE I

THE REVERSIBLE HEAT COEFFICIENT, dV_{OC}/dT VS. STATE-OF-CHARGE (SOC).

SOC (%)	0.9	0.8	0.7	0.6	0.5	0.4	0.3	0.2	0.1
dV_{oc}/dT (V/K)	-0.0001	0.0004	0.0007	0.0003	0.0002	-0.0003	-0.0004	-0.0006	-0.00004

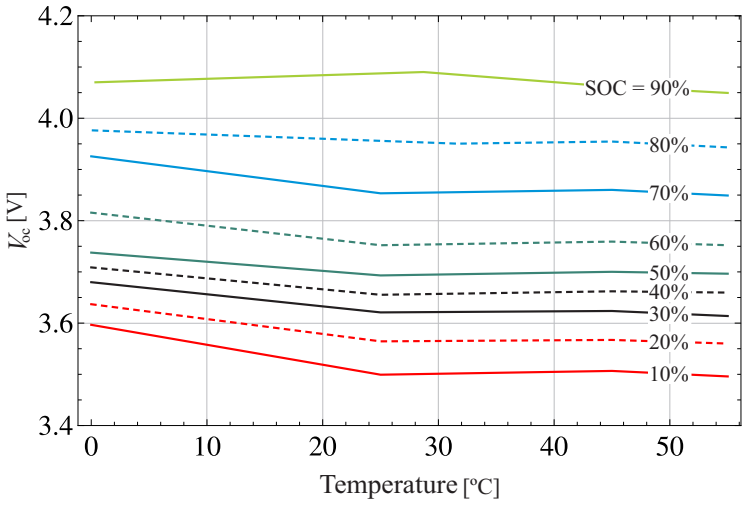

where i_x and i_y are the components of in-plane current density on each electrode obtained from the electrical model; see Eq. (2).

The last term in Eq. (18) takes account for the volumetric heat dissipation to the ambient from x-y plane. The heat dissipation flux q_{diss} is calculated from Newton's law of cooling

$$q_{\text{diss}} = 2h_{\text{eff}}(T_{\text{s}} - T_0) \qquad (21)$$

where T_0 is the constant ambient temperature, T_{s} is the surface temperate, and h_{eff} is the effective heat transfer coefficient ($\text{W m}^{-2}\,\text{K}^{-1}$) at the surface of the cell (both front and back surfaces in x-y plane).

The thermal boundary conditions for the energy balance equation [cf. Eq. (16)] are

$$-\kappa_{\text{eff}}\frac{\partial T}{\partial x} = \left[\frac{\delta_{\text{case}}}{\kappa_{\text{case}}} + \frac{1}{h_{x,0}}\right]^{-1}(T - T_0) \quad \text{at} \quad x = 0 \qquad (22a)$$
$$+\kappa_{\text{eff}}\frac{\partial T}{\partial x} = \left[\frac{\delta_{\text{case}}}{\kappa_{\text{case}}} + \frac{1}{h_{x,a}}\right]^{-1}(T - T_0) \quad \text{at} \quad x = a \qquad (22b)$$
$$-\kappa_{\text{eff}}\frac{\partial T}{\partial y} = \left[\frac{\delta_{\text{case}}}{\kappa_{\text{case}}} + \frac{1}{h_{y,0}}\right]^{-1}(T - T_0) \quad \text{at} \quad y = 0 \qquad (22c)$$
$$+\kappa_{\text{eff}}\frac{\partial T}{\partial y} = \left[\frac{\delta_{\text{case}}}{\kappa_{\text{case}}} + \frac{1}{h_{y,c}}\right]^{-1}(T - T_0) \quad \text{at} \quad y = c \qquad (22d)$$

where δ_{case} and κ_{case} are the thickness and the thermal conductivity of the battery case; see Table II. The convective heat transfer coefficients are denoted by h ($\mathrm{W\,m^{-2}\,K^{-1}}$) with relevant subscripts which indicate the location of the boundary. The initial temperature of the battery is assumed

TABLE II
THICKNESS, THERMAL CONDUCTIVITY, AND ELECTRICAL CONDUCTIVITY OF BATTERY COMPONENTS.

Material/Layer	Thickness, δ (m)	Thermal conductivity, κ ($\mathrm{W\,m^{-1}\,K^{-1}}$)	Electrical conductivity, σ ($\mathrm{S\,m^{-1}}$)
Aluminum current collector	20×10^{-6}	238	37.8×10^{6}
Copper current collector	14×10^{-6}	398	59.6×10^{6}
Separator sheet	25×10^{-6}	0.34 (wet)	-
Positive active material	106×10^{-6}	1.58 (wet)	13.9 (wet)
Negative active material	111×10^{-6}	1.04 (wet)	100 (wet)
Pouch (case)	162×10^{-6}	0.16	-

to be the ambient temperature

$$T = T_0 \quad \text{at} \quad t = 0 \tag{23}$$

III. EXPERIMENTAL

We use a high-power prismatic Li-ion battery (AllCell Technologies, USA) as the experimental battery, with the nominal capacity of 75 Ah. With reference to Fig. 1, dimensions of current collectors in the battery and their electrical conductivity are given in Table. III. The battery core (electrode stack) contains 42 pairs of positive and negative electrodes connected in parallel; nickel-cobalt-manganese cathode and graphite anode. With reference to Fig. 2, electrode dimension in $x-y$ plane are listed in Table III.

TABLE III
DIMENSIONS OF ELECTRODE DOMAINS Ω_p AND Ω_n IN x-y PLANE, CORRESPONDING TO FIG. 2.

Electrode	a (m)	b (m)	c (m)	e (m)
Positive	248×10^{-3}	80×10^{-3}	229×10^{-3}	60×10^{-3}
Negative	248×10^{-3}	80×10^{-3}	229×10^{-3}	188×10^{-3}

Constant-current discharge rates at 1C-rate (75 A), 2C-rate (150 A), 3C-rate (225 A), and 4C-rate (300 A) were performed to measure the battery voltage, V during discharge processes at different environmental temperature of -10, 0, 25, 40, and 55 °C. Each discharge test was performed with the battery uninsulated, lying flat on a perforated plastic rack in an environmental chamber (Envirotronics, ST-27) set at the targeted temperature. Before discharging, in order to establish a 100% state-of-charge, the battery was charged following the constant-current and constant-voltage (CC-CV) protocol, i.e., it was charged at 37.5 A until reaching 4.2 V, then held at 4.2 V until the charging current decreased to 3.75 A. The fully charged cell was then allowed to rest for an hour before a discharging test begins. Voltage data were recorded at a rate of $1\,\mathrm{S\,s^{-1}}$ over the duration of the tests. The cutoff voltage for discharge tests set to 2.7 V. To allow a discharged battery to return to the desired ambient temperature and reach its electrochemical equilibrium, a minimum of four hours elapsed between the end of a discharge cycle and the beginning of the charge cycle.

Additionally, the HPPC test was performed at four different temperature of 0, 25, 45, and 55°C inside the environmental chamber. All discharge tests were performed with a multi-channel power cycler (Arbin Instruments, BT-2000).

IV. RESULTS AND DISCUSSION

Equations in Section II which govern the electro-thermal performance of the cell, form a nonlinear system and must be solved numerically. A finite element PDE solver, COMSOL MULTIPHYSICS (Version 4.3a) (24), is used to simultaneously solve the governing equations over two separated domains, Ω_p and Ω_n, to obtain: i) the transient fields of potential on each electrode and ii) temperature profile in the cell assembly. The developed ECM as a zero-dimensional model is applied to each grid element of the Ω_p and Ω_n domain to account for the effect of the local temperature variation on the ECM parameters and consequently on the voltage and heat distributions. The ECM parameters, see Fig. (**?**), are implemented as look-up tables and the bilinear interpolation technique is applied to find out the value of the ECM parameters at a point (T, SOC) where the experiment data does not exit,

Once the potential distribution on positive and negative electrodes is obtained, the voltage, V, can be calculated from Eq. (6). In Fig. 7, voltage response of the battery at different discharge rates (1 C, 2 C, 3 C, 4 C) and temperature (-10°C, 0°C, 25°C, 40°C, 55°C) is compared to experimental voltage values. The experimental discharge curves agree well with those obtained from the modeling at different environmental temperatures. The discharge curves in Fig. 7 show that the discharge capacity of the cell drops significantly as the temperature decreases below 0°C. At low temperature the activation energy needed for chemical reactions to occur is higher. The intercalation and deintercalation mechanism at the electrodes need more energy, therefore fewer lithium ions can participate in the active cell process. This leads to a temporary capacity loss. Moreover, low intercalation and deintercalation means a lower cell voltage, which influences the deliverable power from the battery. Nonetheless, the above-mentioned effects are temporary; when the temperature is restored to the desirable level, the capacity and power capabilities are recovered (25).

The surface average temperature of the cell calculated from Eq. (24), is plotted in Fig. 8 as a function of discharge time.

$$T_{\text{Ave}} = \int_0^a \int_0^c T(x,y,t)\,\mathrm{d}x\,\mathrm{d}y \tag{24}$$

Plots a-e are intended to assess the temperature effect, where battery is discharge at 2 C (150 A), 3 C (225 A), and 4 C (300 A) rates in an environment of -10°C, 0°C, 25°C, 40°C, and 55°C. The agreement between the model and experiment is acceptable, except a slight discrepancy for plots a and b where the cell is operated at 0 and -10°C environments. There is a hypothesis that the difference between the predicted and measured data is caused by the high sensitivity of the battery performance to operating conditions at subfreezing temperatures. Note that, since the cell voltage is lowered with decrease of temperature [see Fig. 7], especially at subzero temperatures, cell temperature rise is more marked at a lower ambient temperature due to the higher cell resistance and larger voltage loss.

The sensitivity of the discharge performance of the cell at subzero ambient to the heat transfer condition is investigated in Fig. 9, in which the voltage and temperature profiles of the cell simulated at different convective cooling conditions, are plotted against time. Four heat transfer conditions including: adiabatic ($h = 0\,\mathrm{W\,m^{-2}\,K^{-1}}$), $h = 10\,\mathrm{W\,m^{-2}\,K^{-1}}$, $h = 50\,\mathrm{W\,m^{-2}\,K^{-1}}$, and $h = 100\,\mathrm{W\,m^{-2}\,K^{-1}}$ are considered at the ambient of -10°C. Figure 9 shows that at subfreezing environment, by decreasing the convective cooling coefficient, the cell capacity increases by 10%. The low heat transfer coefficient at -10°C, implies large cell resistance, and stronger electro-chemical and thermal interaction that leads to a higher temperature rise, and larger performance boost, which is more noticeable near adiabatic conditions (where h approaches zero). In other words, when the cell is operated at sub ambient temperature, the lower the heat transfer coefficient, h, the higher the discharge capacity can be delivered owing to the faster temperature rise; the BTMS should be able to modulate its cooling power at such environment. Hence, designing an efficient BTMS is necessary to regulate the batteries cooling or heating conditions according to climate conditions.

V. Summary and Conclusions

In this work the authors intended to develop and validate a transient electro-thermal model that can be applied as a tool for design and optimization of BTMS. The following steps were taken to develop and validate the present model:

- a large Li-ion battery pouch (75 Ah) was characterized experimentally to obtain its ECM model which enabled us to simulate the current-voltage characteristic of the battery across variety of operating conditions,
- a coupled electro-thermal model was formulated to calculate the voltage and temperature profile of the battery during the battery operation,
- the ECM, as a zero-dimensional model, was applied to each grid element of the electro-thermal model's geometry.

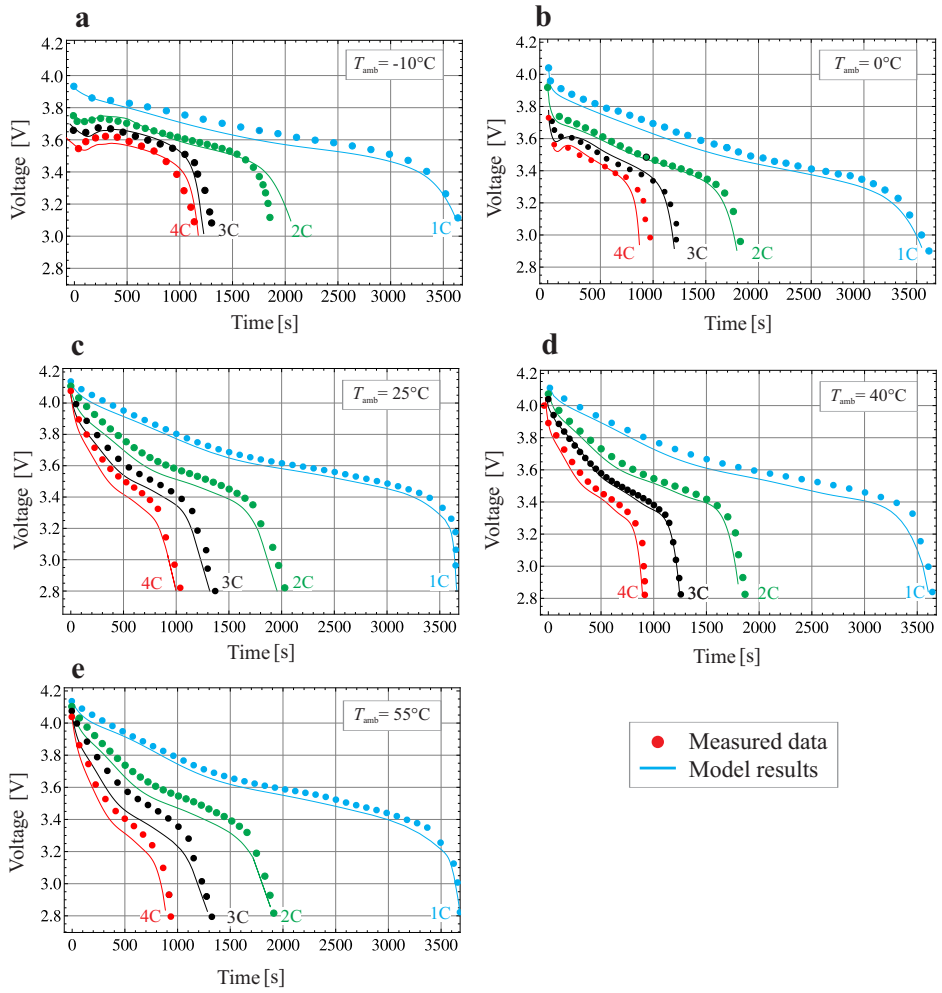

Fig. 7. The variation of battery voltage vs. time at discharge rates of 1 C (75 A), 2 C (150 A), 3 C (225 A), 4 C (300 A) at a) -10°C, b) 0°C, c) 25°C, d) 40°C, and e) 55°C. Symbols correspond to measured values and lines represent calculated values.

- developed model was validated through comparison with the experimental studies.

The validated model was applied to investigate the effect of convective cooling coefficient on the transient thermal response of the battery operating at sub-ambient temperature. Since the working temperature range of the most of the commercial Li-ion battery is between -10°C to 50°C, the simulation was conducted at an ambient of -10°C , as the lower limit. The results show that at such ambient condition, the lower the heat transfer coefficient, h, the higher the discharge capacity can be delivered, owing to the faster temperature rise. This implies that the design of an adaptive BTMS that is capable of regulating its cooling power according to the ambient condition is essential, especially for large scale application of Li-ion batteries.

The presented model can be extended to transient CFD analysis of a large-scale battery pack, which is necessary for designing battery cooling system. In addition, this multi-physics model it has potential to be extended to various applications such as external shorts or nail-penetration.

ACKNOWLEDGMENT

This research was financially supported by the Automotive Partnership Canada (APC), Grant No. APCPJ 401826-10.

BATTERY GLOSSARY

- C-rate: The charge and discharge current of a battery is measured in C-rate. Most portable batteries are rated

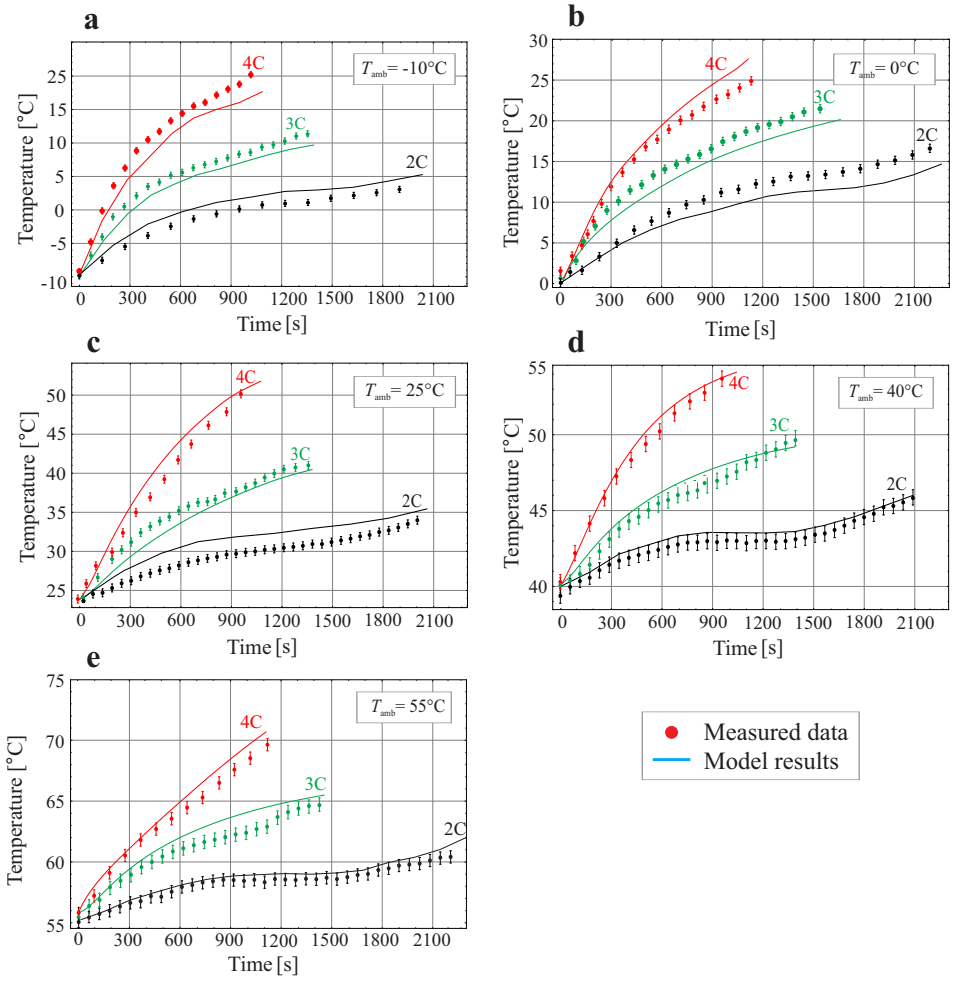

Fig. 8. The variation of battery voltage vs. time at discharge rates of 1 C (75 A), 2 C (150 A), 3 C (225 A), 4 C (300 A) at a) -10°C, b) 0°C, c) 25°C, d) 40°C, and e) 55°C. Symbols correspond to measured values and lines represent calculated values.

at 1 C. This means that a 20 Ah battery would provide 20A for 1 hour if discharged at 1 C rate. The same battery discharged at 0.5 C (1/2 C) would provide 10 A ($20 \times 0.5 = 10$) for 2 hours. 1 C is often referred to as a 1 hour discharge,

- State-of-charge (SOC): The state of charge refers to the amount of charge in a battery relative to its predefined full and empty states i.e. the amount of charge in Amp-hours left in the battery. Manufacturers typically provide voltages that represent when the battery is empty (0% SOC) and full (100% SOC). SOC is generally calculated using current integration to determine the change in battery capacity over time,
- Open circuit voltage (OCV): The open circuit voltage (OCV) is the voltage when no current is flowing in or out of the battery, and, hence no reactions occur inside the battery. OCV is a function of state-of-charge and is expected to remain the same during the life-time of the battery. However, other battery characteristics change with time, e.g. capacity is gradually decreasing as a function of the number of charge-discharge cycles,
- Nominal capacity: The coulometric capacity, the total Amp-hours available when battery is discharged at a certain discharge current (specified as a C-rate) from 100% SOC to the cut-off voltage. Capacity is calculated by multiplying the discharge current (in Amps) by the discharge time (in hours) and decreases with increasing C-rate,

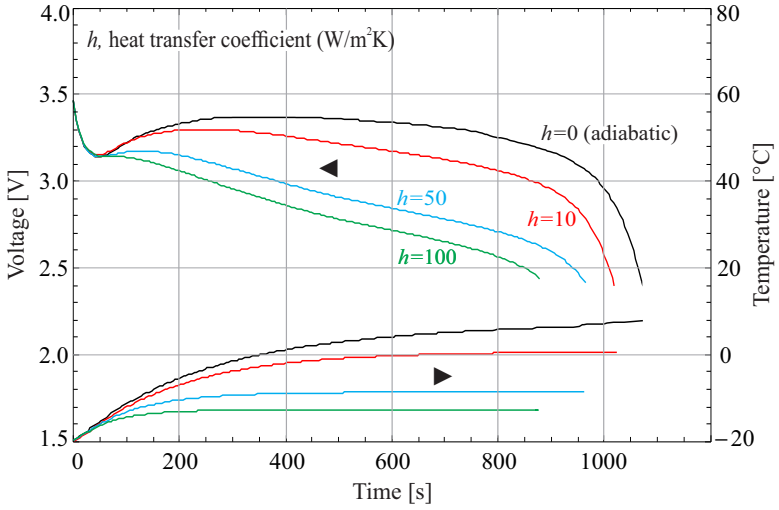

Fig. 9. Effect of heat transfer coefficient on the temperature and voltage profiles of the cell operates at 3 C discharge process and -10°C. The battery performance is simulated at four different heat transfer conditions, including: adiabatic ($h = 0\,\mathrm{W\,m^{-2}\,K^{-1}}$), $h = 10\,\mathrm{W\,m^{-2}\,K^{-1}}$, $h = 50\,\mathrm{W\,m^{-2}\,K^{-1}}$, and $h = 100\,\mathrm{W\,m^{-2}\,K^{-1}}$.

- Cut-off voltage: The minimum allowable voltage. It is this voltage that generally defines the empty state of the battery.

NOMENCLATURE

a	width of electrode (m)
b	width of tab (m)
C	capacitance (F)
c	height of electrode (m)
c_p	specific heat capacity ($\mathrm{J\,kg^{-1}\,K^{-1}}$)
e	distance of tab centre from y-axis (m)
$\dot{g}$	heat generation rate ($\mathrm{W\,m^{-3}}$)
$\dot{g}_{\mathrm{ohmic}}$	ohmic heat generation rate ($\mathrm{W\,m^{-3}}$)
h	heat transfer coefficient ($\mathrm{W\,m^{-2}\,K^{-1}}$)
i	in-plane current density ($\mathrm{A\,m^{-2}}$)
I	applied discharge current (A)
J	reaction current density ($\mathrm{A\,m^{-2}}$)
$\mathbf{n}$	unit normal vector on electrode
N	number of cell assemblies inside the battery core
q	in-plane heat flux ($\mathrm{W\,m^{-2}\,K^{-1}}$)
q_{diss}	heat dissipation flux ($\mathrm{W\,m^{-2}}$)
Q	capacity (A h)
R	resistance (Ω)
t	time (s)
T	temperature (°C)
T_0	ambient and initial temperature (°C)
V	potential (V)
V_{oc}	open-circuit potential (V)
$\mathscr{V}$	volume of battery core ($\mathrm{m^3}$)
x	horizontal position (m)
y	vertical position (m)
BTMS	battery thermal management system
Li-ion	lithium-ion battery

Greek

δ	thickness (m)
κ	thermal conductivity ($\mathrm{W\,m^{-1}\,K^{-1}}$)
ν	volume ratio
ρ	density of cell assembly ($\mathrm{kg\,m^{-3}}$)
Φ	voltage (V)
σ	electrical conductivity ($\mathrm{S\,m^{-1}}$)

Subscript

am	related to active material
batt	related to battery
case	related to battery case
cc	related to current collector
cell	related to cell (electrode pair)
ec	related to electrochemical reaction
eff	related to current collector
elec	related to electrode
n	related to the negative domain
p	related to the positive domain
ss	related to separator sheet
x	related to x-direction
y	related to y-direction

REFERENCES

[1] F. He, H. Wang, L. Ma, Experimental demonstration of active thermal control of a battery module consisting of multiple li-ion cells, International Journal of Heat and Mass Transfer 91 (2015) 630 – 639.

[2] C. Zhang, S. Santhanagopalan, M. A. Sprague, A. A. Pesaran, Coupled mechanical-electrical-thermal modeling for short-circuit prediction in a lithium-ion cell under mechanical abuse, Journal of Power Sources 290 (2015) 102 – 113.

[3] Temperature-dependent electrochemical heat generation in a commercial lithium-ion battery, Journal of Power Sources 247 (2014) 618 – 628.

[4] J. Yi, U. S. Kim, C. B. Shin, T. Han, S. Park, Three-dimensional thermal modeling of a lithium-ion battery considering the combined effects of the electrical and thermal contact resistances between current collecting tab and lead wire, J. Electroche. Soc. 160 (2013) A437–A443.

[5] W. Fang, O. J. Kwon, C.-Y. Wang, Electrochemicalthermal modeling of automotive li-ion batteries and experimental validation using a three-electrode cell, International Journal of Energy Research 34 (2010) 107–115.

[6] G. H. Kim, K. Smith, K. J. Lee, S. Santhanagopalan, A. Pesaran, Multi-domain modeling of lithium-ion batteries encompassing multi-physics in varied length scales, J. Electrochem. Soc. 158 (2011) A955–A969.

[7] M. W. Verbrugge, R. S. Conell, Electrochemical and thermal characterization of battery modules commensurate with electric vehicle integration, J. Electrochem. Soc. 149 (2002) A45–A53.

[8] Y. G. B. Y. Y. Hu, S. Yurkovich, Electro-thermal battery model identification for automotive applications, J. Power Sources 196 (2011) 449–457.

[9] H. Gu, Mathematical analysis of a Zn/NiOOH cell, J. Electrochem. Soc. 130 (1983) 1459–1464.

[10] P. Taheri, A. Mansouri, M. Yazdanpour, M. Bahrami, Theoretical analysis of potential and current distributions in planar electrodes of lithium-ion batteries, Electrochimica Acta 133 (2014) 197 – 208.

[11] P. Taheri, S. Hsieh, M. Bahrami, Investigating electrical contact resistance losses in lithium-ion battery assemblies for hybrid and electric vehicles, J. Power Sources 196 (2011) 6525–6533.

[12] M. Yazdanpour, P. Taheri, A. Mansouri, M. Bahrami, A distributed analytical electro-thermal model for pouch-type lithium-ion batteries, Journal of The Electrochemical Society 161 (2014) A1953–A1963.

[13] M. Guo, R. E. White, A distributed thermal model for a li-ion electrode plate pair, J. Power Sources 221 (2013) 334 – 344.

[14] J. Newman, W. Tiedemann, Potential and current distribution in electrochemical cells: Interpretation of the half-cell voltage measurements as a function of reference-electrode location, J. Electrochem. Soc. 140 (1993) 1961–1968.

[15] Y. Hu, S. Yurkovich, Y. Guezennec, B. Yurkovich, Electro-thermal battery model identification for automotive applications, Journal of Power Sources 196 (2011) 449 – 457.

[16] X. Hu, S. Li, H. Peng, A comparative study of equivalent circuit models for li-ion batteries, Journal of Power Sources 198 (2012) 359 – 367.

[17] D. K. S. Jung, Multi-dimensional modeling of large-scale lithium-ion batteries, Journal of Power Sources 248 (2014) 498–509.

[18] L. Saw, Y. Ye, A. Tay, Electro-thermal characterization of lithium iron phosphate cell with equivalent circuit modeling, Energy Conversion and Management 87 (2014) 367 – 377.

[19] The Idaho National Laboratory is a U.S. Department of Energy National Laboratory, Idaho Operations Office: Idaho Falls, ID, USA; 2010, Battery Test Manual For Plug-In Hybrid Electric Vehicles (2008).

[20] D. R. Baker, M. W. Verbrugge, Temperature and current distribution in thin film batteries, J. Electrochem. Soc. 146

(1999) 2413–2424.

[21] Y. Ye, L. H. Saw, Y. Shi, K. Somasundaram, A. A. Tay, Effect of thermal contact resistances on fast charging of large format lithium ion batteries, Electrochimica Acta 134 (2014) 327 – 337.

[22] M. DOYLE, J. NEWMAN, Analysis of capacityrate data for lithium batteries using simplified models of the discharge process, Journal of Applied Electrochemistry 27 (1997) 846–856.

[23] D. Bernardi, E. Pawlikowski, J. Newman, A general energy balance for battery systems, J. Electrochem. Soc. 132 (1985) 5–12.

[24] COMSOL Multiphysics, www.comsol.com, Stockholm, Sweden.

[25] Y. Ji, Y. Zhang, C.-Y. Wang, Li-ion cell operation at low temperatures, Journal of The Electrochemical Society 160 (2013) A636–A649.